Method for Measuring Surface Charge on Insulating Materials Based on the Vibrating Capacitor Method

Jiaming Fan and Xuefeng Xu *

School of Technology, Beijing Forestry University, Beijing 100083, China; sunnyfjm03@bjfu.edu.cn
* Correspondence: xuxuefeng@bjfu.edu.cn; Tel.: +86-1391-020-5091

Abstract: The phenomenon of surface charging, known as contact electrification or tribocharging, has wide-ranging applications but also notable hazards. Precisely measuring surface charge density in insulating materials is crucial for optimizing tribocharging and mitigating adverse effects. Although the vibrating capacitor method is commonly used for this purpose, its principle, designed for conductive materials, limits direct application to insulating surfaces, leaving the relationship between measured surface potential and surface charge density unclear. To address this issue, this study simulated the process of measuring the surface potential of insulating materials using Comsol simulations. It analyzed the effects of charged area size, probe height, and probe position, and utilized the spatial distribution of potential measurement values of surface point charges to derive an integral relationship between the distribution of measured surface potential values and the distribution of surface charge density. The integral relationship of surface potential distribution under different forms of surface charge density distributions calculated from this formula largely matches the numerical simulation results. Based on this, a relationship between the distribution of surface charge density and surface potential measurement values was further derived. This relationship can be used for measuring the surface charge density of insulating materials.

Keywords: vibrating capacitor method; surface charge density; Triboelectrification; electrostatic field simulation

1. Introduction

The phenomenon of surface charging induced by mutual contact and friction between materials is referred to as contact electrification or triboelectrification [1–5]. This process involves the transfer of charges, leading to the accumulation of charges of different polarities and densities on the surface of objects, resulting in electrostatic effects. Although static electricity plays a positive role in various fields such as electrostatic dust removal [6–9], electrostatic spraying [10–13], electrostatic flocking [14–17], and electrostatic copying [18,19], the accumulation discharge of charges and electrostatic attraction also pose significant hazards. For example, electrostatic discharge may cause electromagnetic interference and circuit breakdown in electronic devices [20,21], high-voltage electrostatic discharge poses a threat to personal safety [22], and electrostatic discharge in dusty environments may lead to explosions and fires [23–25]. Additionally, dust adhesion caused by electrostatic attraction can significantly reduce the quality of industrial products [26]. Therefore, precise measurement of the surface charge density of objects becomes crucial for better understanding and controlling electrostatic effects, achieving safer, more efficient, and reliable applications.

Currently, various methods exist for measuring the surface charge density of materials. Wang et al. [27] utilized electrostatic induction to derive the relationship between the contact separation distance and the surface charge density by measuring the voltage of the circuit during the contact separation process. Furthermore, by measuring the voltage of the same liquid metal after the contact separation with the tested material, the contact electrification charge density of different materials for the same material can be inferred.

The Faraday cup method records the change in current when the tested material enters the Faraday cup through electrostatic induction to calculate the quantity of charge, thereby obtaining the charge density [28,29]. The aforementioned methods provide the average surface charge density of materials and cannot reveal the distribution characteristics of charge density on the surface. Electrostatic field strength meters can measure electric field strength, which can then be used to deduce the charge distribution [30]. This method does not require direct contact with the material, thus avoiding interference with the tested material. However, the spatial resolution of electrostatic field strength meters is often limited and cannot accurately calculate the surface charge density of materials.

In 1898, Lord Kelvin invented a technique for measuring the contact potential difference of metals, known as the Kelvin method [31]. In 1932, Zisman optimized this method by designing circuits to make it more sophisticated and accurate [32–35]. The Kelvin method is also known as the vibrating capacitor method. In this method, the contact potential difference between two metals is generated due to the different work functions of the metals [36–38]. A capacitor is formed between the probe and the tested metal, and by applying vertical vibration to the probe perpendicular to the test surface, the contact potential difference induces a weak current in the measuring circuit. Applying a certain bias voltage to the probe ensures no current flows in the measuring circuit. At this point, the probe-to-ground voltage equals the material's contact potential difference. Later, the vibrating capacitor method was used to measure the surface potential of dielectric materials. As the probe size decreased, the spatial resolution of surface potential measurement improved. Subsequently, the Kelvin method was combined with Atomic Force Microscopy (AFM) technology, gradually developing into Kelvin Probe Force Microscopy (KPFM) technology, achieving atomic-level spatial resolution in surface potential measurement. In KPFM technology, by applying DC and AC biases to the probe, the DC bias is used to compensate for the surface potential of the sample, while the AC bias generates changing electrostatic forces to make the probe vibrate. When the second harmonic amplitude of the probe is zero, the DC bias applied to the probe equals the surface potential of the material.

Currently, the vibrating capacitor method can achieve non-contact and non-destructive measurement of surface potential with high spatial resolution, serving as the theoretical basis for many commonly used surface potential measurement devices. However, the vibrating capacitor method was originally designed to detect the contact potential difference or differences in work functions of samples. During the measurement process, the stable current parameters ensure that the applied bias voltage strictly equals the potential difference between the tested metal and the reference voltage. However, unlike conductors, dielectric materials do not have a fixed and uniform surface potential. In addition to being related to surface charge polarity, density, and other conditions, the surface potential of dielectric materials is also influenced by factors such as probe size, probe position, and probe bias voltage [39–42]. Conversely, due to their extremely low conductivity, the surface charge distribution of dielectric materials often remains stable. Therefore, the surface potential of dielectric materials does not have physical significance; what can be stably measured is their surface charge density. However, so far, the quantitative relationship between the surface potential measurement values obtained by the vibrating capacitor method and the surface charge density remains unclear, affecting the accurate measurement of surface charge density of dielectric materials.

This study proposes a method based on Comsol simulations to establish the relationship between surface charge and measured voltage for dielectric materials, while simplifying the simulation process through integration calculation. The aim of this paper is twofold: firstly, to establish an ideal parallel plate capacitor theoretical model and derive the theoretical relationship between surface charge density and measured potential. Additionally, the study aims to create two-dimensional and three-dimensional simulation models of the vibrating capacitor method measurement process. It also investigates the influence of factors such as charged area and probe height on the measured potential using COMSOL Multiphysics 5.6. Lastly, the study seeks to establish an analytical relationship between

the measured potential value and the surface charge density distribution. This is based on the potential measurement model of surface point charge distribution. The feasibility of integration calculation as an alternative to simulation methods is then validated using various charge density distributions, including circular trajectory sinusoidal distribution, circular trajectory random distribution, square region random distribution, and others.

2. Methods and Simulation

2.1. Simulation Model

Based on the working principle of the vibrating capacitor method and the structural characteristics of the probe, this study establishes a simulation model using Comsol software. Two models are adopted for the charged region shape. In the contact-separation frictional charging process, a circular charged region with uniform charge distribution is selected. For the rotational friction process, a ring-shaped charged region with varying charge density is chosen.

According to the characteristics of the two charged region shapes mentioned above, we respectively establish two-dimensional axisymmetric models and three-dimensional models. The established two-dimensional axisymmetric model represents the circular charged region and mainly includes two geometric entities: the probe and the tested dielectric material. As shown in Figure 1a, the probe is a cylinder with a height of 1 mm and a radius of 2 mm. The tested dielectric material is cylindrical with a radius of 145 mm and a height of 5 mm. These two entities are coaxially arranged, and the lower surface of the probe is kept 2 mm away from the upper surface of the dielectric material. The three-dimensional model is designed for the ring-shaped charged region. To simulate the charge distribution, the ring is divided into 12 subregions, each with a uniform charge distribution. Similarly, there are two parts: the probe and the tested dielectric material, as shown in Figure 1b. The geometric characteristics of the probe are consistent with the above two-dimensional model; namely, a cylinder with a height of 1 mm and a radius of 2 mm. The tested dielectric material is cylindrical with a height of 5 mm and a bottom radius of 15 mm. The probe is located directly above the ring with an outer diameter of 11 mm and an inner diameter of 9 mm, maintaining a distance of 2 mm from the upper surface of the tested dielectric material. In both models, an external computational domain surrounds a region with a thickness of 10 mm, which serves as an infinite element domain. The infinite element domain approximates an infinite domain by using grids with extremely low densities to replace grids at far distances.
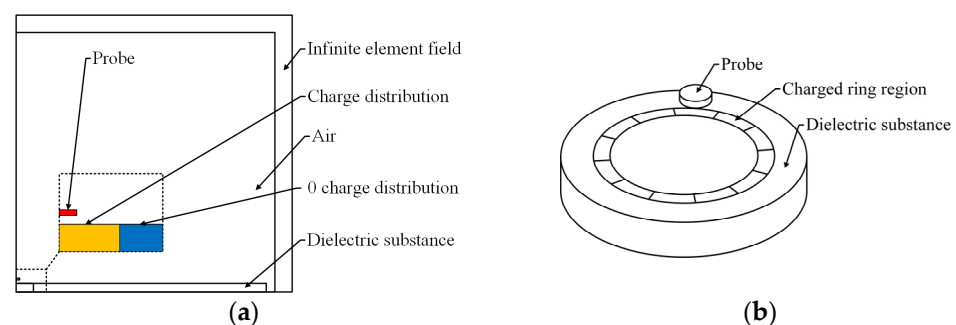

(**a**)	(**b**)

Figure 1. Simulation geometric model: (**a**) 2D axisymmetric model; (**b**) 3D model.

Under the combined effect of bias voltage and surface charge of the sample, the probe generates induced charges on its surface. By performing steady-state electrostatic field simulations at the upper and lower limit positions of the probe's vibration, the surface charge quantities at these two extreme positions are obtained. The difference between them represents the change in surface charge. When the change in surface charge is zero, the voltage applied to the probe corresponds to the surface potential measurement value.

2.2. Boundary Conditions and Material Parameters

In the configuration of the physical field, steady-state calculations are performed using Comsol Multiphysics with the AC/DC electrostatic interface. For the two-dimensional axisymmetric model, the boundary conditions are set as follows: charge conservation throughout the entire air region. Charge conservation within the tested dielectric material. The lower surface of the tested dielectric material is grounded. The upper surface of the tested dielectric material is divided into two regions: one region with uniform surface charge density, and the other region with zero charge density. The probe is set as a terminal, allowing for the application of voltage. In the three-dimensional model, the boundary conditions are set as follows: charge conservation throughout the entire air region. Charge conservation within the tested dielectric material. The lower surface of the tested dielectric material is grounded. The upper surface of the tested dielectric material is divided into a ring-shaped region, uniformly subdivided into 12 equal parts, as shown in Figure 1b. Applying different charge densities to these regions can simulate uniform charge distribution similar to the ring-shaped region, point charge distribution, and sinusoidal characteristic charge distribution. The remaining regions are set as zero-charge regions. The probe is set as a terminal, allowing for the application of voltage.

The material parameters remain consistent across both models. Copper has been selected as the material for the probe. Its linear resistivity is specified as 1.72×10^{-8} Ω·m, while conventionally, its relative permittivity is set to 1. However, for metallic materials, the relative permittivity tends towards infinity. Consequently, in the software, this value is adjusted to 10^{10}. The dielectric material subjected to testing is polytetrafluoroethylene (PTFE), characterized by a relative permittivity of 2. The remaining constituents are represented by air, with a relative permittivity of 1.

2.3. Mesh Independence Verification

To ensure the stability and accuracy of the results, mesh independence verification is conducted during the mesh generation stage. In both the two-dimensional and three-dimensional models, mesh refinement is gradually performed near the probe. With an increase in the number of refinement iterations, the results gradually stabilize, indicating that further mesh reduction would not significantly affect the computational results. As shown in Figure 2a,b, it is evident that additional mesh refinement does not significantly affect the results when the initial two-dimensional probe mesh size is 0.005 mm. Therefore, the current mesh is considered suitable for subsequent calculations. Similarly, for the three-dimensional probe mesh with a size of approximately 0.05 mm, further mesh reduction does not significantly impact the computational results, allowing for the utilization of the existing mesh for subsequent calculations.
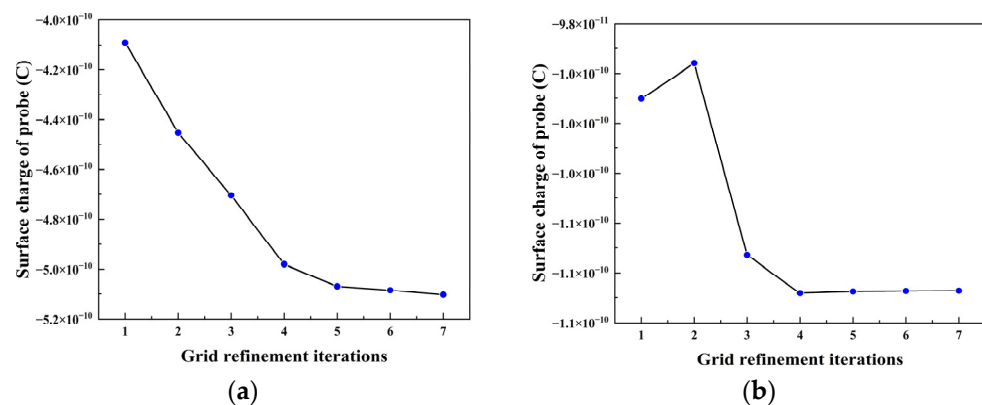

Figure 2. Curve diagram of model mesh insensitivity: (**a**) mesh insensitivity of 2D axisymmetric model; (**b**) mesh insensitivity of 3D model.

To ensure the stability and accuracy of the results, mesh independence verification is conducted during the mesh generation stage. In the two-dimensional model, a free triangular mesh is selected as the mesh unit, with gradual mesh refinement near the probe. In the three-dimensional model, a free tetrahedral mesh is chosen as the mesh unit, and gradual mesh refinement is also performed near the probe. As the number of refinement iterations increases, the results gradually stabilize, indicating that further mesh reduction would not significantly affect the computational results. As shown in Figure 2a,b, additional mesh refinement does not significantly affect the results when the initial two-dimensional probe mesh size is 0.005 mm. Therefore, the current mesh is considered suitable for subsequent calculations. Similarly, for the three-dimensional probe mesh with a size of approximately 0.05 mm, further mesh reduction does not significantly impact the computational results, allowing for the utilization of the existing mesh for subsequent calculations.

3. Results and Discussion

3.1. Theoretical Model of Parallel Plate Capacitor

Based on the principle of the vibrating capacitor method, a theoretical model is established, as shown in Figure 3. σ_{in} represents the surface charge density of the dielectric material sample, caused by phenomena such as frictional charging, and remains unaffected by other variables during the measurement process. σ_1 denotes the induced surface charge density on the lower surface of the upper metal plate (probe) after applying the input voltage, while σ_2 represents the surface charge density induced on the lower metal plate (sample holder) and the lower surface of the insulating material sample.
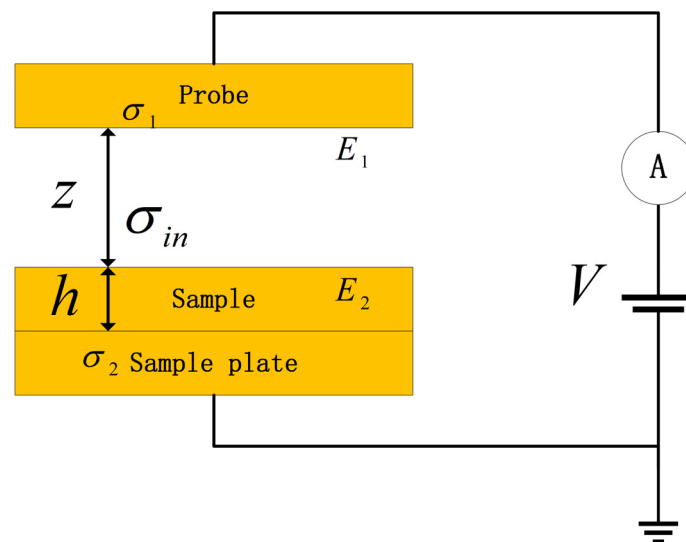

Figure 3. Parallel plate capacitor model with dielectric material.

In addition, let z denote the distance between the lower surface of the probe and the upper surface of the sample, and h represent the thickness of the sample being measured. E_1 represents the magnitude of the electric field between the probe plates, while E_2 denotes the electric field within the sample. V represents the voltage output from the voltage source, and A denotes the inclusion of an ammeter in series within the circuit.

Therefore, in electrostatic equilibrium, the applied voltage provided by the external circuit satisfies the following equation for potential measurement. In the equation, ε_0 represents the vacuum permittivity and ε_r represents the relative permittivity of the dielectric material:

$$V = E_1 z - E_2 h = \frac{\sigma_1}{\varepsilon_0} z + \frac{\sigma_1 + \sigma_{in}}{\varepsilon_0 \varepsilon_r} h \tag{1}$$

$$\sigma_1 = \frac{\varepsilon_0 \varepsilon_r V - \sigma_{in} h}{\varepsilon_r z + h} \tag{2}$$

By adjusting the magnitude of the potential measurement to ensure that the current in the circuit is zero, we achieve:

$$\frac{\partial \sigma_1}{\partial z} = 0 \tag{3}$$

At this point, the relationship between the surface charge density of the material and the potential measurement is:

$$\sigma_{in} = \frac{\varepsilon_0 \varepsilon_r V}{h} \tag{4}$$

Formula (4) represents the relationship between the surface charge density of the sample and the measured voltage in the ideal state of the parallel plate capacitor model.

3.2. Relationship between Measured Potential and Charged Area

When the tested material is a dielectric substance, due to its low conductivity, surface charges adhere to the material surface. Different measured potentials exist at different distances between the probe and the charges. Therefore, by establishing a two-dimensional axisymmetric model as shown in Figure 1a, with the lower surface of the probe maintained at a distance of 2 mm from the upper surface of the tested material, when the surface charge density of the charged region is set to 7.08×10^{-6} C/m^2 as σ_{ex}, the results, as shown in Figure 4, indicate that the measured potential rapidly increases within a radius of 10 mm as the charged area gradually increases from a radius of 0.5 mm to the entire lower surface with a radius of 145 mm uniformly distributing positive charges. When the radius of the charged area is 10 mm, the measured potential value approaches a peak of 3438.75 V. After the radius of the charged area exceeds 10 mm, the measured potential gradually decreases, reaching close to 2000 V as the charged radius reaches its maximum. According to Formula (4) in the parallel plate capacitor model, it can be calculated that the measured voltage is 2000 V when the lower surface of the tested material carries the currently set surface charge density under ideal conditions. It can be observed that the measured potential in the simulation experiment gradually approaches the theoretical value as the radius of the charged area increases. Furthermore, it is found that when the charge density is constant, the measured potential of the area with a radius of 10 mm is significantly greater than that of the entire lower surface with uniformly distributed charges. We speculate that this phenomenon, where a region with a smaller charge quantity exhibits a larger measured potential, is due to edge effects caused by uneven electric field line distribution.
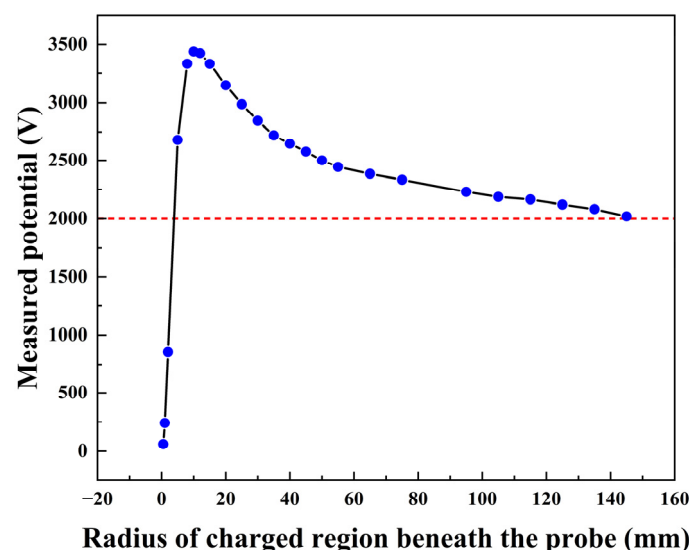

Figure 4. Relationship between measured potential and size of charged region below the probe.

3.3. Relationship between Measured Potential and Probe Height

According to the principle of the vibrating capacitor method, for conductors, theoretically, the measured potential does not change with variations in the probe height. However, when the tested material is a dielectric substance, there is no clear correspondence between the material surface charge and the measured potential. Therefore, in the two-dimensional axisymmetric model, the entire upper surface of the tested material is uniformly charged with σ_{ex} and the edge of the tested material approaches an infinite domain. The distance between the lower surface of the probe and the sample is gradually adjusted. As shown in Figure 5a, it can be observed that the measured potential remains stable at around 2000 V as the distance between the probe and the sample increases from 2 mm to 7 mm. Thus, under ideal conditions, when the charged region attached to the tested material approaches infinity, the measured potential of this model is not affected by changes in the probe height. However, for dielectric materials, charges can stably adhere to fixed positions. When the region below the probe is a charged area with a radius of 10 mm and a charge density of σ_{ex}, the measured potential exhibits a stable linear relationship as the distance between the probe and the sample increases from 2 mm to 6 mm, as shown in the following figure. This indicates that for dielectric materials under ideal conditions, the vibrating capacitor method model requires strict limitation of the probe height.
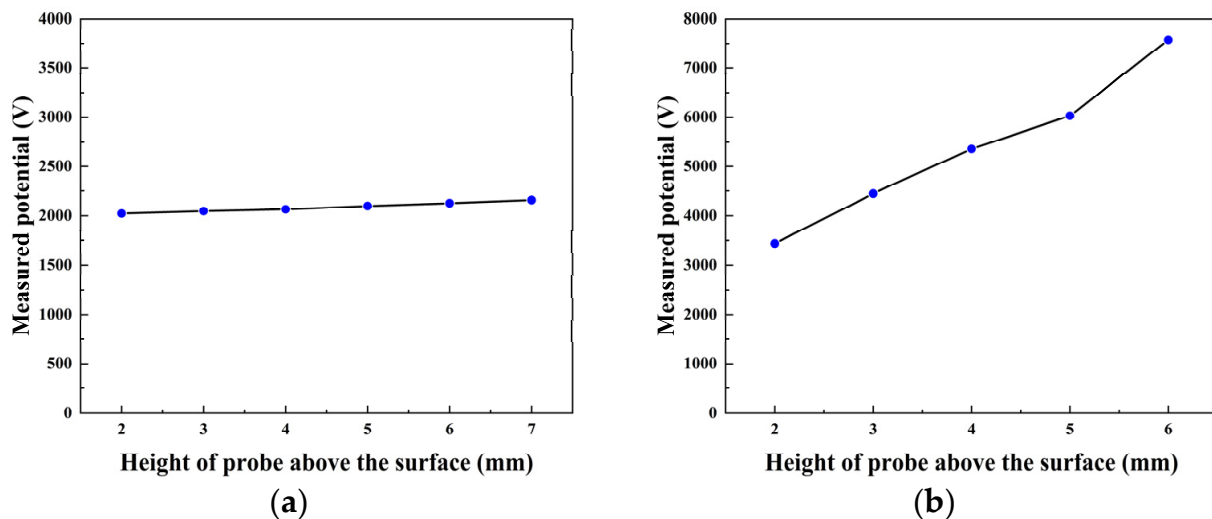

Figure 5. Relationship between measured potential and probe distance: (**a**) overall charged surface of the material; (**b**) locally charged.

3.4. Relationship between Measured Potential and Charge Density Distribution

During the process of measuring surface potential using the vibrating capacitor method, the measured potential may be influenced by surface charges outside the measurement position. In order to establish the relationship between measured potential and surface charge density, simulations are first conducted to calculate the measured potentials at different positions under a point charge density distribution. Considering the influence of probe height on the surface charge of dielectric materials, the distance between the probe and the material surface is strictly maintained at 2 mm. Surface charges at different distances will result in different measurement values of potential. Therefore, in the three-dimensional model, a circular point charge area with a diameter of 1 mm is established at the center of the surface of the dielectric material. The probe is gradually moved horizontally from directly above the initial point charge area, with each movement being 2 mm. The results are shown in Figure 6.
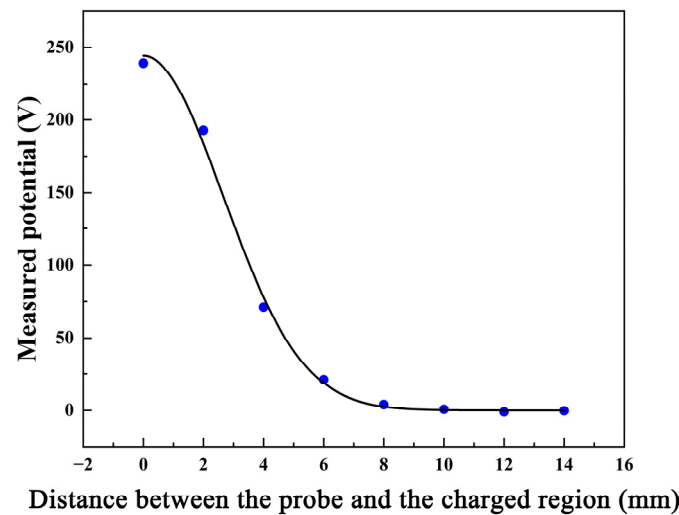
Figure 6. Relationship between measured potential and distance to charged region.

It can be observed that as the probe gradually moves away from the tested charged area, the measured potential of the probe rapidly decreases and approaches 0 volts. Through fitting, we can obtain the formula for the measured potential value V_0 as a function of the horizontal distance x between the center of the probe and the center of the charged area as follows:

$$V_0 = 244.37 \times e^{-\frac{x^2}{14}} \tag{5}$$

After normalization, the formula can be derived as follows, where r in the equation represents the linear distance between the tested unit charge and the center of the probe.

$$V = \frac{244.37C/V \times e^{-\frac{r^2}{14}}}{\pi \times 1mm \times 1mm \times 7.08 \times 10^{-6}C/m^2} \tag{6}$$

where r in the equation represents the linear distance between the tested unit charge and the center of the probe. The relationship between the linear distance and the horizontal distance x and the vertical distance y is as follows:

$$r^2 = x^2 + y^2 \tag{7}$$

When the probe is placed above any charged region, the measured potential values for different charged regions can be calculated using the formula:

$$V(x,y) = \iint \sigma(x',y') \times \frac{244.37C/V \times e^{-\frac{(x-x')^2+(y-y')^2}{14}}}{\pi \times 1mm \times 1mm \times 7.08 \times 10^{-6}C/m^2} dx'dy' \tag{8}$$

The term V (x, y) in the equation represents the measured voltage at the unit coordinates (x, y), while σ (x', y') denotes the magnitude of the surface charge density at the coordinates (x', y'). The measured potential value at the current position can be obtained by performing the integration calculation of the charged region using the above formula based on the surface charge density under different conditions.

3.5. Validation of Different Types of Charge Density Distributions

Various scenarios of charge distribution have been investigated to validate distinct charging models. For example, during material contact and separation, surface charges often exhibit point-like characteristics. In our friction experiments, periodic friction along a circular trajectory may yield sinusoidal voltage measurements. Moreover, charges confined within localized regions may display random distribution properties. Through the exami-

nation of these diverse scenarios, our objective is to evaluate the feasibility of employing integration calculations as an alternative to simulation methods.

For the point charge region within the circular ring friction area, one of the 12 regions in Figure 1b is selected to set the surface charge density to σ_{ex}, while the remaining regions are set to $0\,C/m^2$. The probe initially moves away from the charged region to other regions.

The results are shown in Figure 7a: The x-coordinate of the probe section represents the position of the probe. As shown in Figure 1b, when the probe is directly above the charged region, the x-value is 1. When the probe is positioned above an adjacent region next to the charged region, the x-value is 2, and so on. Since only one region is charged, and the entire model exhibits symmetry, it is only necessary to measure half of the circular ring area; namely, probe section 1 to 7. It can be seen that as the probe moves away from the charged region, the measured potential rapidly decreases and gradually approaches 0 V. Moreover, the simulation results of the model are close to the results of the integration calculation. In tribological experiments, after repeated cyclic friction in circular regions, measurements of surface charge along the friction trajectory exhibit characteristics reminiscent of sinusoidal signals.
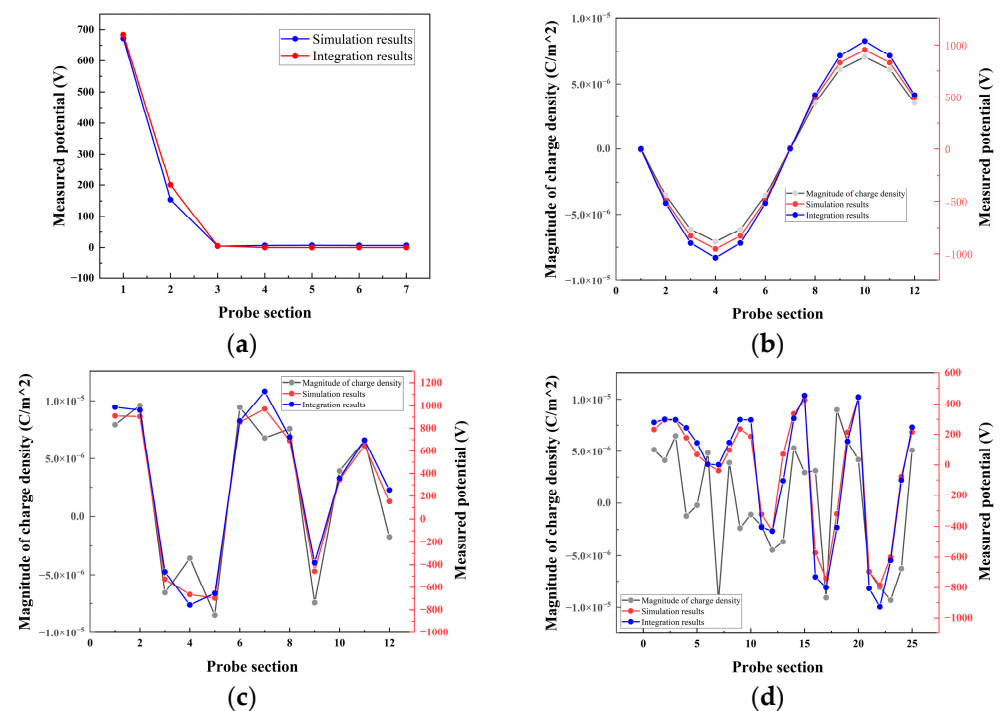

Figure 7. Relationship comparison between simulation models and integral calculation results: (**a**) region with point charge distribution along circular trajectory; (**b**) region with sine feature charge distribution along circular trajectory; (**c**) region with random feature charge distribution along circular trajectory; (**d**) region on the surface of a rectangle with random feature charge distribution.

When the charge distribution characteristic is similar to the friction experiment, surface charge densities with sinusoidal distribution characteristics are sequentially set in the 12 regions in Figure 1b. The probe measures each charged region in sequence. The results, as shown in Figure 7b, demonstrate that the simulation model results are very close to the numerical results obtained from the integrated calculations.

For the case of charges randomly distributed on the surface of the dielectric material, 12 random numbers representing the surface charge density in each subregion of the circular ring area are generated. The corresponding measured potentials are solved using both simulation methods and formula integration calculations, as shown in Figure 7c. The gray line represents the randomly generated surface charge density values below the probe area, while the red and blue lines represent the simulated measured potential values obtained

using the Comsol model and the calculated values obtained using the formula, respectively. Although there may be some fluctuations in situations where the surface charge density varies greatly, the curves obtained from both methods are generally consistent with the characteristics of the surface charge density distribution. The calculated values are similar to the simulated values in terms of characteristics, and the numerical values are also close.

However, it is more typical for material surfaces to exhibit irregular and non-uniform surface charges. Hence, in the modified configuration illustrated in Figure 1b, the circular regions with charge are omitted and, instead, the central area of the upper surface is partitioned into 25 square regions with side lengths of 2 mm, forming a 5 × 5 grid. Random numbers are then generated to denote the surface charge density within these 25 regions. Subsequently, the probe systematically scans from directly above the first square to directly above the last square. The resultant measured potentials, obtained through both model simulations and formulaic computations, are depicted in Figure 7d. On the *x*-axis, the probe's position is represented by grid numbers, starting from 1 when situated above the initial grid and incrementing sequentially until 25 as the probe traverses the grid. The *y*-axis denotes the measured voltage corresponding to the probe's position above the current grid. The gray line signifies the randomly generated surface charge density values beneath the probe area, while the red and blue lines respectively denote the simulated measured potential values derived from the simulation model and the calculated values obtained using the formula.

Observations from the graphical representations indicate that, for instances where the charge distribution exhibits relatively simple characteristics, such as point charge or sinusoidal distribution, the measured voltages obtained through integration calculations closely mirror those derived from simulations, with a minor numerical variance of approximately 50 V. However, in scenarios featuring more random charge distributions, while the measured voltages obtained through integration calculations demonstrate similar characteristics to simulation results, there are notable numerical differences, reaching approximately 100 V. Nevertheless, the overall trends in the measured voltages from both methods remain consistent. Notably, increasing the granularity of partitioning within the charged region may potentially yield more precise outcomes, as it enhances the model's ability to capture nuanced features of the charge distribution, thus reducing discrepancies in measured voltages. However, it is important to emphasize that while greater partitioning may enhance accuracy, the primary focus of this study remains the proposition of a method leveraging integration calculations to optimize complex simulations, thereby achieving computational cost savings.

4. Conclusions

This research successfully addressed the challenge of measuring surface charge density in insulating materials using Comsol simulation methods. By analyzing parameters such as charged area size, probe height, and position, and utilizing the spatial distribution of potential measurement values of surface point charges, an integral relationship closely associated with the distribution of surface charge density was established. Validation against numerical simulation results from four common charge distribution scenarios confirmed the feasibility of using this integral relationship calculation method to replace complex electrostatic field simulation processes for determining the relationship between surface charge density and measured voltage. Additionally, this method provides a reliable approach for measuring surface charge density in insulating materials. These findings contribute to a deeper understanding of contact electrification phenomena and offer practical applications in fields such as material science, electronics, and energy storage.

The vibrating capacitor method, as a non-contact and high-precision technique for measuring electric fields, exhibits promising prospects in various domains including electronic devices and material analysis. By accurately exploring the actual surface charge distribution characteristics of materials, a better understanding of material properties and device design can be achieved, thereby providing new avenues for technological advancement. Although

significant progress has been made in this research, there are still limitations. Due to constraints in experimental conditions, it is currently challenging to accurately determine the charge density on a material surface. Future studies will explore the utilization of KPFM experimental equipment for microscopic-scale experiments to refine the theoretical framework. Additionally, further optimization of the vibrating capacitor method's model and methodology is essential. Practical shielding structures will be integrated to enhance model realism and accuracy. Validation through comparison with alternative methods will be pursued. Furthermore, an in-depth investigation into the effects of various parameters on electric field distribution is warranted to broaden application areas. Refinement of the integral formula is necessary to precisely establish the relationship between surface charge density and measured potential, facilitating seamless conversion. By implementing the vibrating capacitor method in practical scenarios, viable solutions to real-world problems can be offered.

References

1. Lowell, J.; Rose-Innes, A.C. Contact electrification. *Adv. Phys.* **1980**, *29*, 947–1023. [CrossRef]
2. Xu, C.; Zi, Y.; Wang, A.C.; Zou, H.; Dai, Y.; He, X.; Wang, P.; Wang, Y.-C.; Feng, P.; Li, D.; et al. On the Electron-Transfer Mechanism in the Contact-Electrification Effect. *Adv. Mater.* **2018**, *30*, 1706790. [CrossRef] [PubMed]
3. Wang, Z.L.; Wang, A.C. On the origin of contact-electrification. *Mater. Today* **2019**, *30*, 34–51. [CrossRef]
4. Lacks, D.J.; Shinbrot, T. Long-standing and unresolved issues in triboelectric charging. *Nat. Rev. Chem.* **2019**, *3*, 465–476. [CrossRef]
5. Wang, H.; Huang, S.; Kuang, H.; Zhang, C.; Liu, Y.; Zhang, K.; Cai, X.; Wang, X.; Luo, J.; Wang, Z.L. A United Triboelectrification Mechanism for Contacts between All Types of Materials. *Adv. Energy Mater.* **2023**, *13*, 2300529. [CrossRef]
6. Sayyah, A.; Crowell, D.R.; Raychowdhury, A.; Horenstein, M.N.; Mazumder, M.K. An experimental study on the characterization of electric charge in electrostatic dust removal. *J. Electrost.* **2017**, *87*, 173–179. [CrossRef]
7. Panat, S.; Varanasi, K.K. Electrostatic dust removal using adsorbed moisture–assisted charge induction for sustainable operation of solar panels. *Sci. Adv.* **2022**, *8*, eabm0078. [CrossRef] [PubMed]
8. Altıntaş, M.; Arslan, S. Reduction of Dust on Solar Panels through Unipolar Electrostatic Traveling Wave. *Appl. Sci.* **2021**, *11*, 9121. [CrossRef]
9. Hirabayashi, M.; Hartzell, C.; Bellan, P.; Bodewits, D.; Delzanno, G.; Hyde, T.; Konopka, U.; Thomas, E.; Thomas, H.; Hahn, I.; et al. Electrostatic dust remediation for future exploration of the Moon. *Acta Astronaut.* **2023**, *207*, 392–402. [CrossRef]
10. Wan, Y.; Hou, S.; Guo, M.; Fu, Y. Surface Properties of Spray-Assisted Layer-By-Layer ElectroStatic Self-Assembly Treated Wooden Take-Off Board. *Appl. Sci.* **2021**, *11*, 836. [CrossRef]
11. Lee, G.; Sim, J.-H.; Oh, G.; Won, M.; Mantry, S.P.; Kim, D.-S. Electrostatic Spray Deposition of Al-Doped ZnO Thin Films for Acetone Gas Detection. *Processes* **2023**, *11*, 3390. [CrossRef]
12. Wang, J.; Zhang, Y.; Zhang, W.; Fan, Z. Research progress of electrostatic spray technology over the last two decades. *J. Energy Eng.* **2021**, *147*, 03121003. [CrossRef]
13. Hoyer, B.; Sørensen, G.; Jensen, N.; Nielsen, D.B.; Larsen, B. Electrostatic spraying: A novel technique for preparation of polymer coatings on electrodes. *Anal. Chem.* **1996**, *68*, 3840–3844. [CrossRef] [PubMed]
14. Woodruff, F.A. Developments in coating and electrostatic flocking. *J. Coat. Fabr.* **1993**, *22*, 290–297. [CrossRef]
15. Uetani, K.; Ata, S.; Tomonoh, S.; Yamada, T.; Yumura, M.; Hata, K. Elastomeric thermal interface materials with high through-plane thermal conductivity from carbon fiber fillers vertically aligned by electrostatic flocking. *Adv. Mater.* **2014**, *26*, 5857–5862. [CrossRef] [PubMed]

16. McCarthy, A.; Shah, R.; John, J.V.; Brown, D.; Xie, J. Understanding and utilizing textile-based electrostatic flocking for biomedical applications. *Appl. Phys. Rev.* **2021**, *8*, 041326. [CrossRef] [PubMed]

17. McCarthy, A.; John, J.V.; Saldana, L.; Wang, H.; Lagerstrom, M.; Chen, S.; Su, Y.; Kuss, M.; Duan, B.; Carlson, M.A.; et al. Electrostatic flocking of insulative and biodegradable polymer microfibers for biomedical applications. *Adv. Healthc. Mater.* **2021**, *10*, 2100766. [CrossRef] [PubMed]

18. Schaffert, R.M.; Oughton, C.D. Xerography: A new principle of photography and graphic reproduction. *JOSA* **1948**, *38*, 991–998. [CrossRef] [PubMed]

19. Duke, C.B.; Noolandi, J.; Thieret, T. The surface science of xerography. *Surf. Sci.* **2002**, *500*, 1005–1023. [CrossRef]

20. Muttaqi, K.M.; Haque, M.E. Electromagnetic interference generated from fast switching power electronic devices. *Int. J. Innov. Energy Syst. Power* **2008**, *3*, 19–26.

21. Peng, Z.; Shao, Y.; Gao, H.-W.; Wang, S.; Lin, S. High-fidelity, high-performance computational algorithms for intrasystem electromagnetic interference analysis of IC and electronics. *IEEE Trans. Compon. Packag. Manuf. Technol.* **2017**, *7*, 653–668. [CrossRef]

22. Zhang, C.; Liu, S.; Xu, K.; Wei, J.; Ye, R.; Sun, W.; Su, W.; Zhang, A.; Ma, S.; Lin, F.; et al. A novel high latch-up immunity electrostatic discharge protection device for power rail in high-voltage ICs. *IEEE Trans. Device Mater. Reliab.* **2016**, *16*, 266–268. [CrossRef]

23. Glor, M. Electrostatic ignition hazards in the process industry. *J. Electrost.* **2005**, *63*, 447–453. [CrossRef]

24. Ebadat, V. Dust explosion hazard assessment. *J. Loss Prev. Process Ind.* **2010**, *23*, 907–912. [CrossRef]

25. Cheremisinoff, N.P. *Dust Explosion and Fire Prevention Handbook: A Guide to Good Industry Practices*; John Wiley & Sons: Hoboken, NJ, USA, 2014.

26. Ao, C.K.; Jiang, Y.; Zhang, L.; Yan, C.; Ma, J.; Liu, C.; Jiang, Y.; Zhang, W.; Soh, S. Balancing charge dissipation and generation: Mechanisms and strategies for achieving steady-state charge of contact electrification at interfaces of matter. *J. Mater. Chem. A* **2022**, *10*, 19572–19605. [CrossRef]

27. Zhang, C.; Zhou, L.; Cheng, P.; Yin, X.; Liu, D.; Li, X.; Guo, H.; Wang, Z.L.; Wang, J. Surface charge density of triboelectric nanogenerators: Theoretical boundary and optimization methodology. *Appl. Mater. Today* **2020**, *18*, 100496. [CrossRef]

28. Palmieri, J.N.; Goloskie, R. Calibration of 30-cm Faraday Cup. *Rev. Sci. Instrum.* **1964**, *35*, 1023–1026. [CrossRef]

29. He, C.; Bi, X.T.; Grace, J.R. Simultaneous measurements of particle charge density and bubble properties in gas-solid fluidized beds by dual-tip electrostatic probes. *Chem. Eng. Sci.* **2015**, *123*, 11–21. [CrossRef]

30. Noras, M.A.; Pandey, A. Surface charge density measurements. *IEEE Ind. Appl. Mag.* **2010**, *16*, 41–47. [CrossRef]

31. Kelvin, L. Contact electricity of metals. *Philos. Mag.* **1898**, *46*, 82–120. [CrossRef]

32. Danyluk, S. A UHV guarded Kelvin probe. *J. Phys. E Sci. Instrum.* **1972**, *5*, 478–480. [CrossRef]

33. Blott, B.H.; Lee, T.J. A two frequency vibrating capacitor method for contact potential difference measurement. *J. Sci. Instrum. (J. Phys. E)* **1969**, *2*, 785–788. [CrossRef]

34. D'Arcy, R.J.; A Surplice, N. The effects of stray capacitance on the Kelvin method for measuring contact potential difference. *J. Phys. D Appl. Phys.* **1970**, *3*, 482–488. [CrossRef]

35. Zisman, W.A. A new method of measuring contact potential differences in metals. *Rev. Sci. Instrum.* **1932**, *3*, 367–368. [CrossRef]

36. Melitz, W.; Shen, J.; Kummel, A.C.; Lee, S. Kelvin probe force microscopy and its application. *Surf. Sci. Rep.* **2011**, *66*, 1–27. [CrossRef]

37. Palermo, V.; Palma, M.; Samorì, P. Electronic characterization of organic thin films by Kelvin probe force microscopy. *Adv. Mater.* **2006**, *18*, 145–164. [CrossRef]

38. Jakob, D.S.; Wang, H.; Xu, X.G. Pulsed force Kelvin probe force microscopy. *ACS Nano* **2020**, *14*, 4839–4848. [CrossRef] [PubMed]

39. Charrier, D.S.H.; Kemerink, M.; Smalbrugge, B.E.; de Vries, T.; Janssen, R.A.J. Real versus measured surface potentials in scanning Kelvin probe microscopy. *ACS Nano* **2008**, *2*, 622–626. [CrossRef] [PubMed]

40. Luo, G.-N.; Yamaguchi, K.; Terai, T.; Yamawaki, M. Influence of space charge on the performance of the Kelvin probe. *Rev. Sci. Instrum.* **2001**, *72*, 2350–2357. [CrossRef]

41. Nonnenmacher, M.; o'Boyle, M.P.; Wickramasinghe, H.K. Kelvin probe force microscopy. *Appl. Phys. Lett.* **1991**, *58*, 2921–2923. [CrossRef]

42. Salomão, F.C.; Lanzoni, E.M.; Costa, C.A.; Deneke, C.; Barros, E.B. Determination of high-frequency dielectric constant and surface potential of graphene oxide and influence of humidity by Kelvin probe force microscopy. *Langmuir* **2015**, *31*, 11339–11343. [CrossRef] [PubMed]